

Report Title

Nanoscale Transport Optimization

ABSTRACT

A generalized modeling tool has been created that facilitates virtual design of active material systems utilizing nanoscale transport. The construct is bio-mimetic in that the stochastic nature of biological transport proteins is utilized as the basis for transport phenomena. The transport response is then coupled to host response (for instance, elastic deformation of the supporting membrane) via finite element analysis. The advantages of this construct are (1) biological transport phenomena tend to be more complex than engineered transport phenomena, and thus encompass both scenarios, (2) utilizing the finite element coupling enables consideration of any geometrical configuration, and (3) biological transport proteins could in fact be utilized directly in the design of active materials with dial-in stimuli and response. One example case of smart material design is offered in some detail, but the range of possibilities is extraordinary. For instance other possibilities include but are not limited to payload release of a neutralizing agent in the presence of marker stimulus. An illustrative example of the burst scenario is therefore also given some consideration in an example drug delivery implementation.

List of papers submitted or published that acknowledge ARO support during this reporting period. List the papers, including journal references, in the following categories:

(a) Papers published in peer-reviewed journals (N/A for none)

Eric Freeman and Lisa Mauck Weiland, 2008, "High Energy Density Nastic Materials: Parameters for Tailoring Active Response, Journal of Intelligent Material Systems and Structures, Jul 2008.

Number of Papers published in peer-reviewed journals: 1.00

(b) Papers published in non-peer-reviewed journals or in conference proceedings (N/A for none)

Number of Papers published in non peer-reviewed journals: 0.00

(c) Presentations

Number of Presentations: 0.00

Non Peer-Reviewed Conference Proceeding publications (other than abstracts):

Eric Freeman and Lisa Mauck Weiland, 2008, "Applications of Biologically Inspired Membranes," ASME SMASIS, Ellicott City, MD, Oct 28-30, 2008.

Number of Non Peer-Reviewed Conference Proceeding publications (other than abstracts): 1

Peer-Reviewed Conference Proceeding publications (other than abstracts):

Eric Freeman and Lisa Mauck Weiland, "Parametric Studies of a Coupled Transport/Hyperelastic Model For High Energy Density Nastic Materials," ASME-IMECE, Seattle, WA, Nov 2007.

Number of Peer-Reviewed Conference Proceeding publications (other than abstracts): 1

(d) Manuscripts

Number of Manuscripts: 0.00

Number of Inventions:

Graduate Students

<u>NAME</u>	<u>PERCENT SUPPORTED</u>
Eric Freeman	0.75
FTE Equivalent:	0.75
Total Number:	1

Names of Post Doctorates

<u>NAME</u>	<u>PERCENT SUPPORTED</u>
FTE Equivalent:	
Total Number:	

Names of Faculty Supported

<u>NAME</u>	<u>PERCENT SUPPORTED</u>	National Academy Member
Lisa Weiland	0.08	No
FTE Equivalent:	0.08	
Total Number:	1	

Names of Under Graduate students supported

<u>NAME</u>	<u>PERCENT SUPPORTED</u>
FTE Equivalent:	
Total Number:	

Student Metrics

This section only applies to graduating undergraduates supported by this agreement in this reporting period

The number of undergraduates funded by this agreement who graduated during this period:	0.00
The number of undergraduates funded by this agreement who graduated during this period with a degree in science, mathematics, engineering, or technology fields:.....	0.00
The number of undergraduates funded by your agreement who graduated during this period and will continue to pursue a graduate or Ph.D. degree in science, mathematics, engineering, or technology fields:.....	0.00
Number of graduating undergraduates who achieved a 3.5 GPA to 4.0 (4.0 max scale):	0.00
Number of graduating undergraduates funded by a DoD funded Center of Excellence grant for Education, Research and Engineering:	0.00
The number of undergraduates funded by your agreement who graduated during this period and intend to work for the Department of Defense	0.00
The number of undergraduates funded by your agreement who graduated during this period and will receive scholarships or fellowships for further studies in science, mathematics, engineering or technology fields:	0.00

Names of Personnel receiving masters degrees

<u>NAME</u>
Eric Freeman (defense scheduled)
Total Number:

Names of personnel receiving PhDs

<u>NAME</u>

Total Number:

Names of other research staff

<u>NAME</u>

<u>PERCENT SUPPORTED</u>

FTE Equivalent:

Total Number:

Sub Contractors (DD882)

Inventions (DD882)

Final Project Report for Army Award: W911NF-07-1-0045
Lisa Mauck Weiland
Assistant Professor
Mechanical Engineering and Materials Science
University of Pittsburgh

Nanoscale Transport Optimization

Table of Contents

Program Goal (Problem Studied)	(2)
Program Summary	(2)
Modeling Construct	(3)
Model Components	(3)
Example Implementation #1: Creation of a Tailored Active Material	(10)
Example Implementation #2: Pharmaceutical Applications	(21)
Conclusions	(25)
Bibliography	(26)

Program Goal (Problem Studied):

Just prior to the time of inception of this project, the pre-existing DARPA Biocide program had brought to light the utility that would be afforded by the existence of a versatile transport modeling template. Thus, the goal of this program was to create a generalized active transport modeling tool which could be adapted to a range of applications, including of course biocide transport. The potential end applications are broad, and could range over active materials design, vaccine development, fuel cell development, etc.

Program Summary:

A generalized modeling tool has been created that facilitates virtual design of active systems utilizing nanoscale transport. The construct is bio-mimetic in that the stochastic nature of biological transport proteins is utilized as the basis for transport phenomena. The transport response is then coupled to host response (for instance, elastic deformation of the supporting membrane) via finite element analysis. The advantages of this construct are (1) biological transport phenomena tend to be more complex than engineered transport phenomena, and thus encompass both scenarios, (2) utilizing the finite element coupling enables consideration of any geometrical configuration, and (3) biological transport proteins could in fact be utilized directly in the design of active materials with dial-in stimuli and response. One example case of smart material design will be offered in some detail, but the range of possibilities is extraordinary. For instance other possibilities include but are not limited to payload release of a neutralizing agent in the presence of marker stimulus. An illustrative example of the burst scenario is therefore also given some consideration in an example implementation.

The generalized approach employs the governing equation,

$$\frac{dV}{dt} = \overbrace{KA(\sum \sigma_s \pi_s - p)}^{\text{osmotic diffusion}} + \overbrace{\sum \bar{V}_s \frac{d}{dt}(n_s)_i}^{\text{active transport}} \quad (1)$$

where K is the permeability of the membrane supporting the transporters, A is the surface area over which flux occurs, σ_s is the osmotic reflection coefficient, π_s is the osmotic pressure of species S , p is the hydrostatic pressure difference generated by substrate/system elastic response, \bar{V} is the partial molal volume of species S , and $d/dt(n_s)_i$ is a combination of all of the flows in the system. Multiple computational platforms are called upon for input to this governing equation. The hydrostatic pressure p is established by the finite element analysis, while the flows and osmotic pressure are determined from the solution of a stiff set simultaneous of equations, as detailed below.

In order to utilize this construct for a given application, a modest level of baseline data from literature or from experiment is required to calibrate the system (this data was not made available for the biocide case). Once calibrated the model is able to project active response as a function of time. In its current form the response trends are correct (in the “y-axis”); namely the shape of the curve with respect to time is correct, as is the relative time for comparison among similar cases.

To demonstrate the versatility of the approach and as noted above, two example cases are considered: Optimization of a novel active material utilizing biological transport proteins and illustration of burst profiles for pharmaceutical applications.

Modeling Construct:

The basic biological transport protein types considered are Exchangers, Cotransporters, Pumps, and Channels. In nature these transporters penetrate a lipid bilayer membrane as illustrated in Figure 1. Channels are passive transport structures that selectively allow certain ions to travel down their electrochemical gradients. An ion pump is an active transporter that uses the biochemical fuel ATP (adenosine triphosphate) to move selected ions against their electrochemical gradients. The exchangers and cotransporters are secondary active transporters that use the energy from the downhill movement of one species to move another species against its electrochemical gradients.

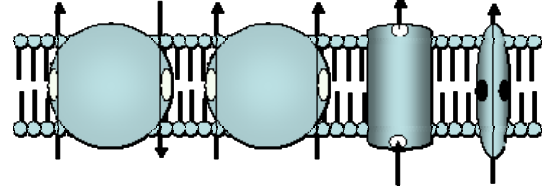


Figure 1. Left to Right, Exchanger, Cotransporter, Pump, and Channel in a bilayer membrane

In nature these transport proteins are typically found in spherical configurations (*i.e.*, vesicles or liposomes) as schematically illustrated in Figure 2. In application (especially engineering application) the configuration may be planar (Fig 1), spherical (Fig 2), or arbitrary. Figure 3 illustrates how the active transport layer may be coupled to an arbitrary surface shape and/or substrate by utilizing finite element analysis. This is accomplished by employing a user defined subroutine for fluid properties at the interface within the finite element package ABAQUS.

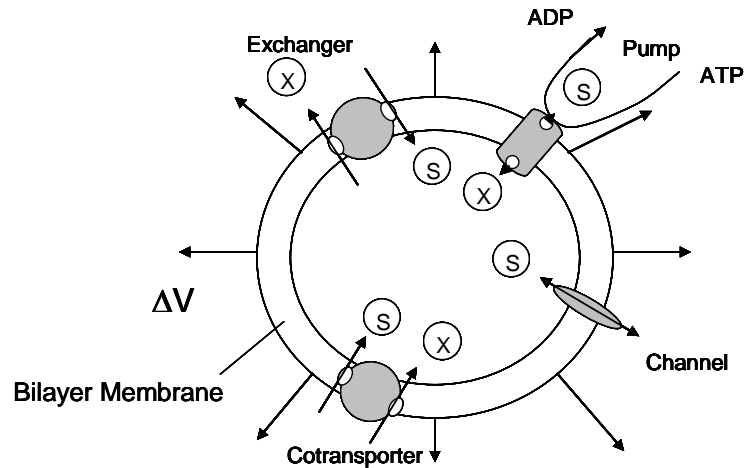


Figure 2. Generalized Vesicle Schematic

Model Components:

As noted above the governing equation for the material system is given as,

$$\frac{dV}{dt} = \overbrace{KA(\sum \sigma_s \pi_s - p)}^{\text{osmotic diffusion}} + \overbrace{\sum \bar{V}_s \frac{d}{dt}(n_s)_i}^{\text{active transport}} \quad (1)$$

The input that feeds into this governing equation includes:

- Membrane potential;
- Membrane diffusion;
- Transport protein activation; and
- Elastic substrate response.

Each of these contributions is described in this section.

Membrane Potential:

As illustrated in Figure 2 the membrane supports the active transport proteins as well as phase separates interior and exterior regions. When the transporters are active, the differing electrochemical state of these regions establishes a potential difference v between the interior and exterior of the membrane,

$$v = v_i - v_e \quad (2)$$

This potential can be approximated through the Hodgkin-Huxley model (Hodgkin, Huxley, and Katz, 1952; Hodgkin and Huxley, 1952). This assumes the membrane is isopotential with evenly distributed transporters across its surface. The number of transporters is assumed large enough that overall behavior of the individual transporter gating events averages out and that each one of the channels do not interact locally. The capacitance of the membrane is charged by ion flux and the establishment of a diffuse double layer at each of the membrane faces (Cevc, G, 1990).

Each type of ion that permeates the membrane is represented by a resistor plus potential sources series connecting the intra and extra-cellular spaces (Figure 4). The resistance through the circuit is determined by the instantaneous effective permeability of the membrane which includes the effects of the channels, pumps, exchangers, and cotransporters.

Using conservation of current principles, the current at the intracellular node (I) is determined to be:

$$I = C \frac{dv}{dt} + \sum i \quad (3)$$

where C is the membrane capacitance and is a measurable material property. The capacitance of most biological membranes is around 1 uF/cm^2 , and ranges from 0.3 and 1.5 uF/cm^2 for the black lipid membranes used in these studies. The actual value is dependent on the presence of organic solvent in the phospholipid tails. (Ries, Choi, Blunck, Nezanilla, et al. 2004). The membrane potential with respect to time may be determined by:

$$\frac{dv}{dt} = -\frac{1}{C} \sum i \quad (4)$$

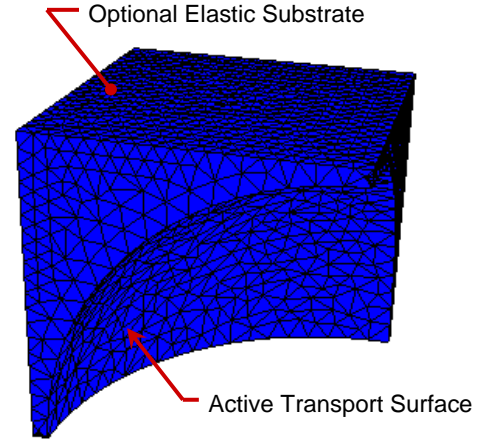


Figure 3. *Coupling Active Transport Layer to a Substrate*

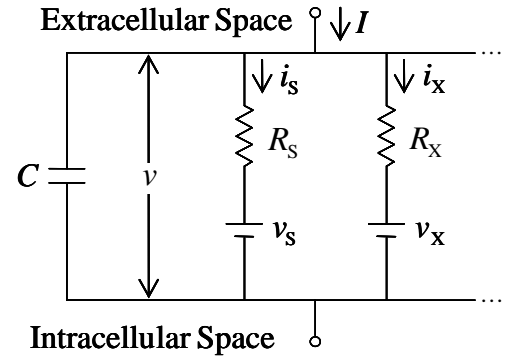


Figure 4. *The Membrane as Capacitance Circuit*

Membrane Electrodifffusion:

In addition to having a capacitive property, the membranes are permeable to small ions. To account for this permeation, the Nernst-Planck equation (1D) may be employed. The In one dimension form (linear), the flux for an ion S is

$$J_s = -u_s c_s \left[RT \frac{d \ln c_s}{dx} + z_s F \frac{d\phi}{dx} \right] \quad (5)$$

where u_s is the mobility of ion S , c_s is the concentration of ion S and is a function of the distance x through the membrane, and ϕ is the electric potential. (Schultz, 1980; Disalvo, Tien, 1989,) This theory of ion flux is commonly used in modeling ion channels and electrodiffusion.

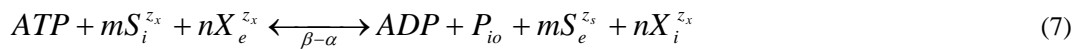
This equation assumes that there is no convective flow, and that the flow is not affected by any other forces or flows. Because determining the flow experimentally is extremely difficult, the flow form is assumed to be based on an assumption about the membrane material such as homogeneity. Therefore, the electric field and gradient of electric potential is assumed to be constant across the membrane. In addition, the species concentration at the intra and extra cellular surfaces is assumed to be a linear function of the species concentration in their corresponding mediums. The linear coefficients (B_s) are assumed to be independent of the species concentration. With these assumptions, the Nernst-Planck equation may be integrated with respect to x to yield (Bonting de pont 1981,)

$$J_s = -\frac{\beta_s u_s F v}{\delta} \left[\frac{[S]_i - [S]_e \exp\left(-\frac{z_s F v}{RT}\right)}{1 - \exp\left(-\frac{z_s F v}{RT}\right)} \right] \quad (6)$$

where $v = \phi(x) - \phi(0)$ is the membrane potential. This equation is also known as the Goldman-Hodgkin-Katz equation. A separate form of the GHK equation is required for each permeable species in the system.

Ion Pumps:

Each of the biological transport proteins may be modeled through determining the chemical reaction rate of that protein. For ion pumps the reaction may be modeled through available ATP free energy, membrane potential, and the equilibrium potentials of the transported ions. The reaction occurring at the pumps is given by,



where m S ions are moved out of the cell and n X ions are moved into the cell in a single cycle. From this, the net current is given by (Endresen 1997)

$$i_{\text{pump}} = k_{\text{pump}} \tanh\left(\frac{e[(-nz_x)v + nz_x v_x] - \Delta G_{\text{ATP}}}{2kT}\right) \quad (8)$$
$$k_{\text{pump}} = (-nz_x)Me\lambda$$

where k_{pump} is a measure of the maximum pump current in cycles/sec, e is the electron charge, v is the membrane potential, z_X is the valence charge of ion X, v_X is the Nernst equilibrium potential for ion X, k is Boltzmann's constant, T is the absolute temperature, M is the number of pumps, λ is the net pump rate (cycles/sec), and ΔG_{ATP} is the free energy released by the breakdown of ATP. The above expressions assume uniform behavior of the pumps across the membrane. In this study proton pumps were used where X represents the proton density, and the pump only transports one species outside of the membrane.

Ion Channels:

Ion channels are modeled per the Nernst-Planck equation, and employ stochastic methods to predict the gating process. The channel gates are assumed to randomly switch between completely open and completely closed states. The gating is influenced by concentration gradients and the overall membrane potential along with a gating mechanism for each channel. The current through these channels is determined by

$$i_s = k_s x \sinh\left(\frac{z_s e(v - v_s)}{2kT}\right) \quad (9)$$

$$k_s = 2z_s e u_s kT \sqrt{[S]_e [S]_i} \frac{A_p}{\varepsilon d}$$

In these equations, $x = x(t)$ is the probability of the channel remaining open. Z_s is the valence charge of the ion S, e is the charge of an individual electron, v is the potential determined by equation 2, k is Boltzmann's constant, T is the absolute temperature, u_s is the ion mobility through the channel, and $[S]$ is the concentration of ion S inside and outside the inclusion, n_s is the number of moles of ion S in the inclusion at time t , A_p is the effective pore area of the ion channel, d is the total channel length, and e_d is the effective pore length of the ion channel where $0 < e < 1$.

The equations used assume that the area is a constant value of A_o except for a short narrow pore in the middle with an area A_p significantly smaller than the channel area. The electric field is also assumed to be constant everywhere inside the channel, and that the current is uniform through the cross sections.

The Nernst equilibrium potential which represents the required membrane potential for the flux of a given ion S to be zero is:

$$v_s = \frac{kT}{z_s e} \ln \frac{[S]_e}{[S]_i} \quad (10)$$

The probability of a channel being open is determined by solving the differential equation for $x(t)$,

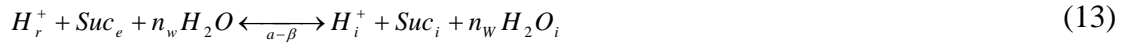
$$\frac{dx}{dt} = \frac{1}{\tau_s \cosh\left(\frac{2e(v - v_x)}{kT}\right)} \left\{ \frac{1}{2} \left[1 + \tanh\left(\frac{2e(v - v_x)}{kT}\right) \right] - x \right\} \quad (11)$$

where t_s is the ion channel relaxation time, which is the amount of time required for channel transition between the open and closed state. For this equation, the energy difference between the two states must be a function of the gating charge q and the difference in energy for both states.

$$\Delta G = q(v_x - v) \quad (12)$$

H⁺/Sucrose Cotransporters:

In the model study, a specific cotransporter was considered, namely the SUT4 H⁺/Sucrose Cotransporter. While a specific cotransporter has been selected because of the ready availability of fitting parameters (from Sundaresan 2005), the construct is adaptable to any cotransport or exchanger type. The reaction for the SUT4 cotransporters used in this study allows for the cotransport of H⁺, Sucrose, and water. The reaction is:



Through relating the forward and backwards reaction rates (α β) to the energy balance from Mullins, Endresen's methodology may be adapted to demonstrate that the current through the cotransporter may be given by:

$$i_{\text{cotransporter}} = k_{\text{cotransporter}} \sinh\left(\frac{e(v - v_H - v_{\text{Suc}} - n_w v_{\text{H}_2\text{O}})}{2kT}\right) \quad (14)$$

$$k_{\text{cotransporter}} = 2Ne\lambda \sqrt{[H^+]_e [H^+]_i [Suc]_e [Suc]_i [H_2O]_e^{n_w} [H_2O]_i^{n_w}}$$

The subscripts 'e' and 'i' denote external and internal concentrations respectively. $[H^+]$ represents the proton concentrations, $[Suc]$ represents the sucrose concentrations, N is the number of cotransporters, $\lambda = \alpha + \beta$ is the sum of the forward and backward reaction rates, and v_{Suc} and $v_{\text{H}_2\text{O}}$ are the sucrose and water potentials respectively, and they are used to simplify the equations.

$$v_{\text{Suc}} = \frac{kT}{e} \ln \frac{[Suc]_e}{[Suc]_i} \quad v_{\text{H}_2\text{O}} = \frac{\bar{V}_{\text{H}_2\text{O}}}{F} \sum \pi_s \quad (15)$$

In the expressions for the sucrose and water potentials, $\bar{V}_{\text{H}_2\text{O}}$ is the partial molal volume of the water, $\sum \pi_s$ is the total osmotic pressure across the membrane, and F is the Faraday constant. Both the sucrose and the water are neutral and thus the potentials have no physical significance. All of these equations assume a rigid stoichiometry between the transported ions, and that either ion can activate the transporter.

Coupling to Elastic Substrate:

In order to capture the response of an engineered actuator the coupling to the actuator system was also required. A finite element methodology employing ABAQUS was employed for this purpose. The constraint of the surrounding substrate material was captured via the Mooney-Rivlin strain energy potential (ABAQUS, 2004).

$$U = C_{10}(\bar{\lambda}_1^2 + \bar{\lambda}_2^2 + \bar{\lambda}_3^2 - 3) + C_{01}(\bar{\lambda}_1^{-2} + \bar{\lambda}_2^{-2} + \bar{\lambda}_3^{-2} - 3) + \frac{1}{D_1}(J_{el} - 1)^2 \quad (16)$$

where U is defined as the strain energy potential of the system where C_{10} , C_{01} , D_1 are material properties, and λ represents deviatoric stretch in the principal directions. For these studies C_{10} and C_{01} were set to values appropriate to a stiff polymer undergoing equibiaxial loading: 89.0 and 0.0 MPa, respectively. Further, the material is treated as nearly incompressible with D_1 set to 9.23E-4 MPa. Because thermal effects are ignored in this analysis, each of these values is treated as a constant. In addition, yielding is not considered in this analysis but could be introduced by replacing the Mooney-Rivlin approach with a strain hardening criterion.

The final output of the model combined ion and solvent flows determined the total solvent flux through the membrane. The solvent flux is a combination of osmotic diffusion and stoichiometric active transport (Su et al 2002).

$$\frac{dV}{dt} = \overbrace{KA(\sum \sigma_s \pi_s - p)}^{\text{osmotic diffusion}} + \overbrace{\sum \bar{V}_s \frac{d}{dt}(n_s)_i}^{\text{active transport}} \quad (1)$$

where K is the permeability of the membrane and A is the surface area over which flux occurs. σ_s represents the osmotic reflection coefficient and π_s is the osmotic pressure of species S . P is the hydrostatic pressure difference generated by ABAQUS. V is the partial molal volume of species S , and $d/dt(n_s)$ is given by:

$$\frac{d}{dt}(n_s)_i = \frac{(-mz_s i_{pump} / (mz_s - nz_x) + az_s i_{exchanger} / (bz_x - az_s) + i_{cotransporter} - i_s - i_{diff})}{z_s F} \quad (17)$$

which is a combination of all of the flows in the system. Lastly, osmotic pressure in a non-ideal solution is given by (Robinson; 1965):

$$\pi_s = \frac{RT}{V_A} \frac{v_s W_A}{1000} ((m_s \phi_s)_i - (m_s \phi_s)_e) \quad (18)$$

where R is the ideal gas constant, T is the absolute temperature, V_a is the partial molal volume of the solution, W_a is the molecular weight of the solution, and $m_s \phi_s$ is the molal concentration of the solution multiplied by an experimentally determined osmotic coefficient. As before, i and e denote the intracellular and extracellular spaces respectively.

Implementation:

In order to predict the effect of coupling an active bilayer membrane (BLM) with an engineered inclusion, the commercial finite element package ABAQUS Standard is employed. The polymer matrix is meshed using hybrid linear 3D tetrahedral continuum elements with the hyperelastic option

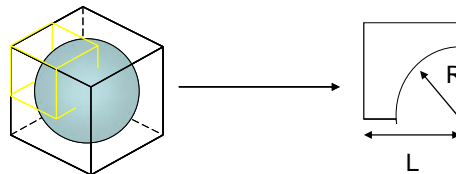


Figure 5. Inclusion Geometry Parameter

(C3D4H); an example meshed system is illustrated in Figure 3. The model is mirrored along all the axes to produce a full spherical inclusion, and a node is generated at the middle of the inclusion. This center node is then constricted and serves as the center for expansion. The active membrane layer is created via hydrostatic fluid elements along the interior of the inclusion; this is accomplished through modifications to the input file. The user-defined program uses DVODE and DOPRI5 methods to solve the stiff matrix of simultaneous equations governing transport at this surface. ABAQUS Standard then uses implicit integration methods to expand the inclusion along a set volume range and determines the pressure generated by the polymer deformation. This Pressure-Volume information is subsequently used to simulate pressure feedback with the UFLUID code. For the example case this pressure response is determined for different inclusion volume fractions, as measured by R/L (Figure 5). Figure 6 illustrates the resulting pressure curves.

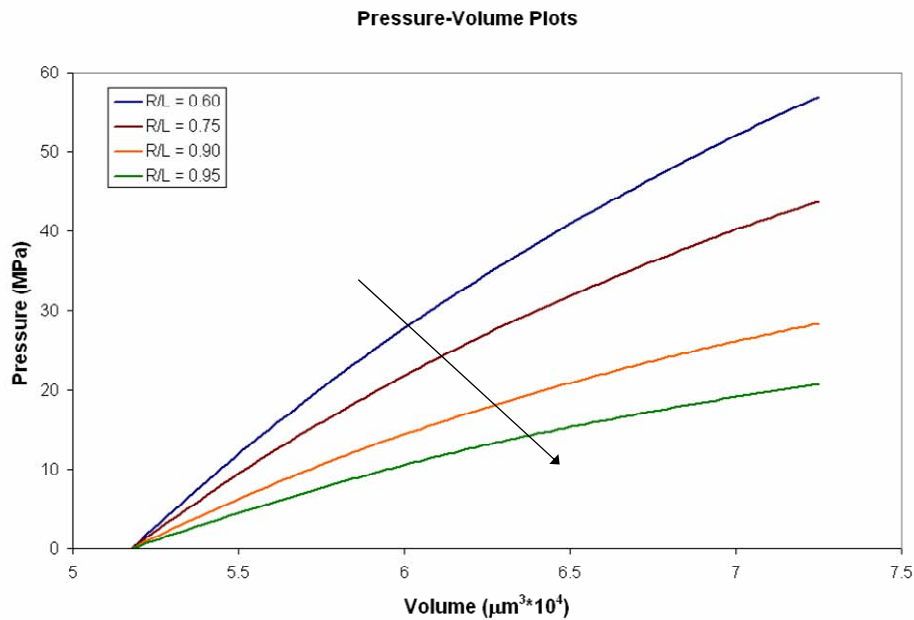


Figure 6. Pressure-Volume Response for Varied R/L Ratios. The arrow indicates the trend for increasing R/L ratio

This methodology allows for considerable customization for a variety of different applications. Further, it could be argued that the advantage of using ABAQUS for this modeling construct has more to do with its ability to impose a user-defined subroutine that solves a complex system of simultaneous equations than the finite element functionality which effectively contributes only one term (p) to the governing equation (Eq 1). Input files govern the properties of the inclusion, and allow the user to control the time limitations of the simulation without modifying the core program itself. This gives the program a degree of flexibility.

Example Implementation #1: Creation of a Tailored Active Material

Consider utilizing the example configuration of Figure 3 where a spherical inclusion is embedded in a host matrix. An array of such inclusions could be selectively stimulated akin to that illustrated in Figure 7. In order to effectively create such a system the behavior of individual inclusions must first be understood. Moreover, the behavior of these inclusions in the context of ‘smart materials’ is required. The classic parameters for this purpose are blocked force, free displacement, and impedance matched work.

To assess these parameters for the engineered active material the definitions are developed in accordance with Figure 8.

Blocked Force Calculations:

While introducing a boundary condition of zero displacement along an edge in a finite element analysis is straight forward, the resultant load at each point along that constrained surface varies with position. In application, an array of these volume elements would experience a blocking force akin to having placed a rigid plate across the blocked surfaces, where the value of interest is the total force required to prevent the displacement of the rigid plate. Quite a number of approaches are available to generate this parameter, with varying degrees of complexity and accuracy; here a rather simple application of thin shelled pressure vessels analysis is adapted for estimating the blocked force.

To implement this approach, the inclusion is approximated as a spherical pressure vessel. Balance of forces dictates that the hoop stress acting on the pressure vessel cross section must balance the internal pressure, resulting in the classic derivation, $\sigma_\theta = pr/2t$. Employing the same approach in the deformed blocked stress state, where the pressure vessel is now oblate, balance of forces may be employed to infer the value of the blocked force required to sustain the blocked configuration.

The values estimated for hoop stress via this method are checked against the free displacement predictions for accuracy; the approach proves to be a reasonable approximation for the R/L cases of 0.75, 0.90, and 0.95. The error associated with the approximation becomes large for the case of $R/L = 0.60$ and this case will not be presented.

Because the dimensions of the model are small, the resulting blocked force values are also small. Thus to better enable direct comparison between these predictions and the behavior of other active materials blocked stress (divide by L^2) results are presented.

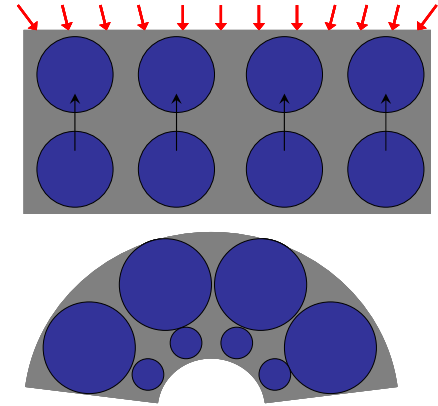


Figure 7. Array Deformation. Arrow indicate ATP stimulation; Transport favors stimulated inclusions

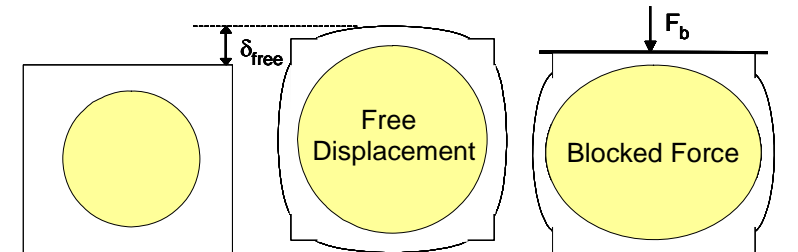


Figure 8. Illustration of Free Displacement and Blocked Force as measured with respect to the undeformed model. Blocked Force assumes load distribution analogous to that imposed with a rigid plate

Free Displacement:

The free displacement as illustrated in Figure 8 is easily determined from the finite element analysis for each case. Because of the small size of the model the parameter is presented in terms of free strain (divide by L) to enable comparison with other active materials.

Impedance Matched Work:

Impedance matched work is given as

$$W = \frac{F_b \delta_{free}}{8} \quad (19)$$

or under the assumption of uniform material response it may be presented on a per unit volume basis as

$$w = \frac{\sigma_b \varepsilon_{free}}{8} \quad (20)$$

where σ_b is blocked stress and ε_{free} is free strain. The expression for impedance matched work per unit volume should provide a reasonable means to anticipate this property in the bulk material. In addition, as a means to enable better understanding of this active material, it is instructive to also consider the work done by the inclusion. With Figure 9 as a reference, this value of work will be calculated as

$$w_{incl} = \frac{(p) \left(\frac{r_f - r_i}{r_i} \right)}{8} \quad (21)$$

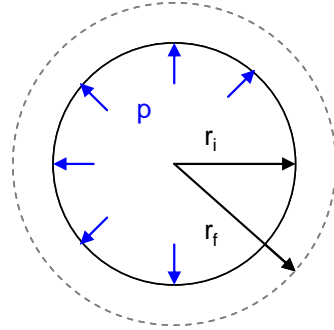


Figure 9. Illustration of Inclusion Work

where p is the peak internal pressure attained for each case, r_i is the initial inclusion radius and r_f is the final inclusion radius.

Predictions of active response will utilize the parameters detailed in Table 1.

Tailored Active Material Predictions

Transient Response:

When considering the transient description of inclusion peak volume and peak pressure (Figure 10), parameters of note are time to peak, time at peak, and relaxation time, which collectively represent the time of the entire transient event. Experimental validation of this modeling approach has demonstrated that the relative shapes of the transient response curves are appropriate, but it is premature to claim high levels of accuracy on the absolute time corresponding to each of these transient responses. Detailed consideration of the total time elapsed for any aspect of response should focus relative performance improvements rather than absolute prediction. Thus for the current state-of-the art, these sequentially occurring time zones are loosely defined.

TABLE 1 – Initialized System Configuration for Experimentally Established Baseline Parameters and Hypothetical Increased Performance Parameters

Parameter	Notation	Units	Baseline	Increased Performance
Int. & ext. pH	$pH_e=pH_{i0}$		5	4
Int. & ext. Sucrose conc.	$[Suc]_e=[Suc]_{i0}$	mM	1.0	5.0
Net Cotrans. Current per transported species*	$N_{SUT4}e\lambda_{SUT4} \cdot ([W]_w^{ne}[W]_i^{nw})^{1/2}$	$pA/(mM H^+) \cdot (mM Suc)$	65	650
Cotransporter H ₂ O Stiochiometry	n_w		350	700
Membrane Capacitance	C	μF	0.105	0.105
Membrane Permeability	K	$\times 10^{-15} m^3/Ns$	1.65	1.65
Membrane Surface Area	A	$\times 10^{-2} (\mu m)^2$	1.57	1.57
Osmotic Reflection	σ		1	1
Max. Ion Pump Current	k_{pump}	pA	65	65
Energy release from ATP hydrolysis	ΔG_{ATP}	$\times 10^{-20} J$	-1.0	-1.5
Membrane Potential	v_o	V	0.0	0.0
Inclusion Volume	V_o	$\times 10^{-4} (\mu m^3)$	5.18	5.18

*There is insufficient experimental data to isolate a maximum cotransporter current; alternatively the lumped value summed over all system cotransporters with respect to transported species can be inferred from experimental data.

Baseline Volume Expansion

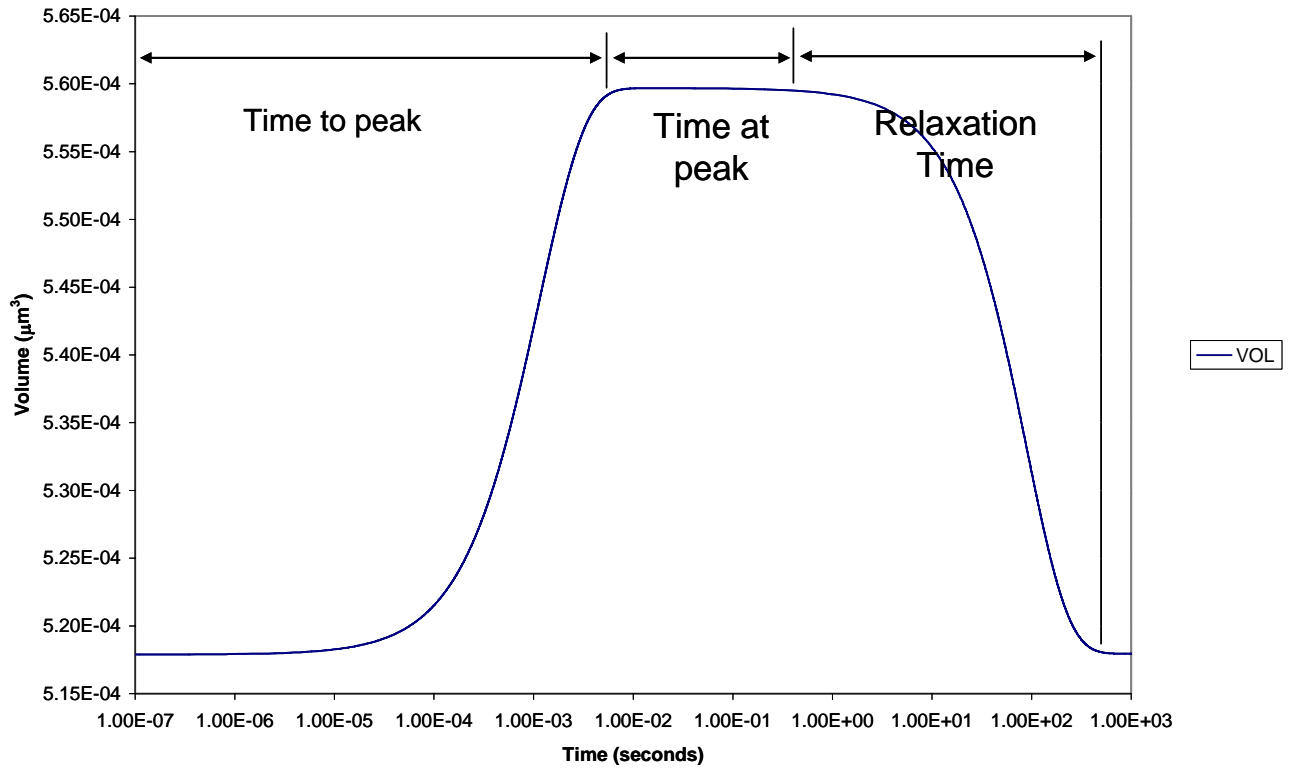


Figure 10 – Illustration of transient values.

Volume Response (Inclusion Only)

For the initialized baseline conditions detailed in Table 1, increased R/L ratios (reducing the surrounding polymer volume) results in modestly increased peak volume and time at peak (Fig 11a). In addition, the final equilibrium volume is modestly increased for increased R/L . The predicted time to peak remains unchanged for each case, while the entire transient event is predicted to occur over ~ 0.1 seconds.

For the Increased Performance input parameters (Fig. 11b), the peak volume response is dominated by the transport side of the reaction; the hyperelastic components have little effect. Because of this a plateau effect is observed, with time to peak significantly faster in comparison to the Baseline case (~ 0.0001 seconds). In addition, the peak itself is significantly increased. After examining the files, it is determined that each simulation reaches the “plateau” at around the same time, however each model continues to expand slowly until a certain point around halfway through its plateau.

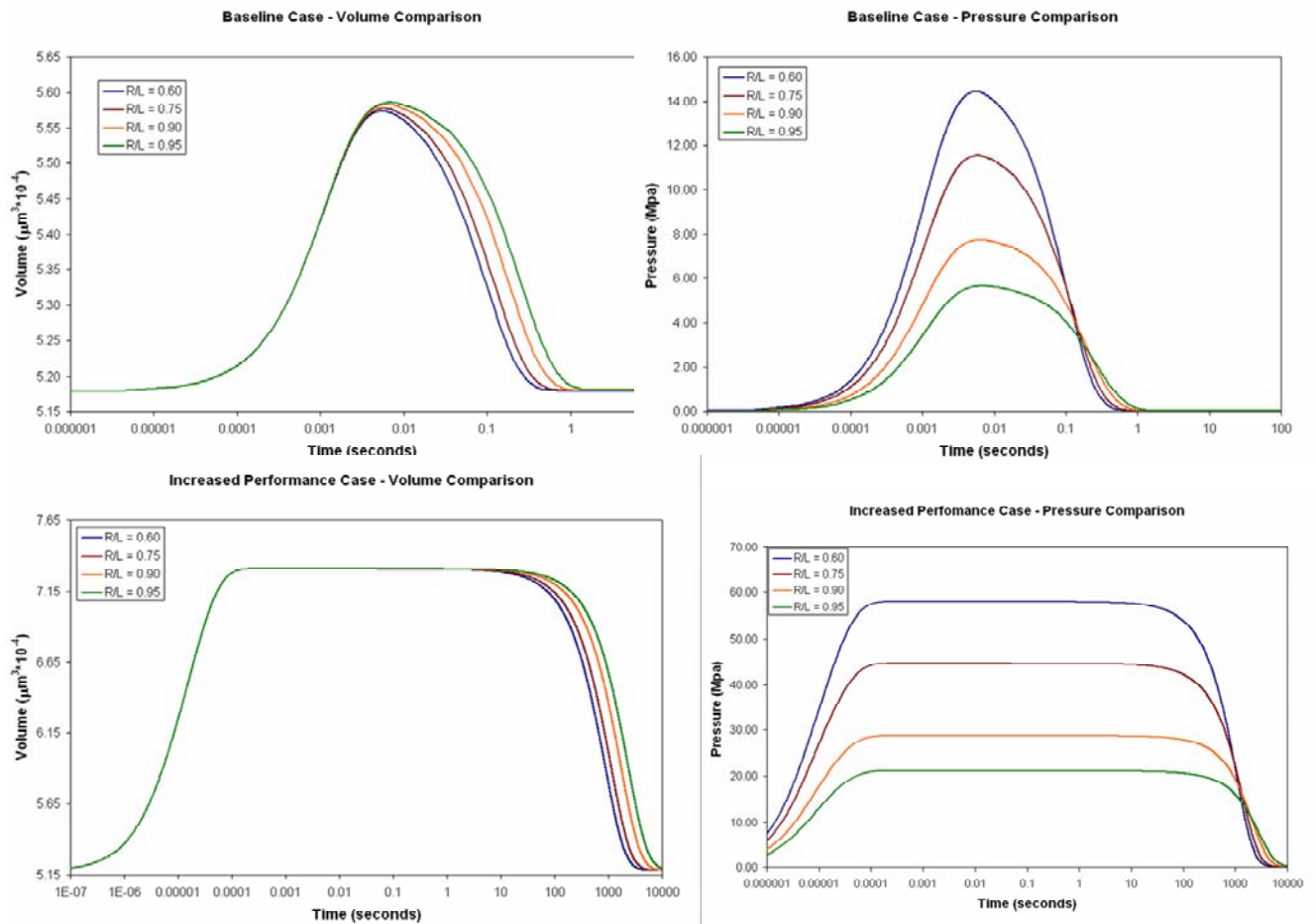


FIGURE 11 A-D – Pressure Volume results for Baseline and Optimized Case

Pressure Response (Inclusion Only)

The pressure transient response is highly dependent on the geometry of the model. (Figs. 11c and 11d). Higher R/L ratios display significantly reduced peak pressure while the time to peak is modestly shorter for decreased R/L ratios.

For the Baseline input parameters the predicted peak pressure is reached more quickly than peak volume (~ 0.0001 seconds), but the total event continues to occur over ~ 0.1 seconds. Thus, the two peaks will coexist at some moment in time. The final equilibrium pressure is identical in all cases.

For the Increased Performance parameters, the peak pressure for each R/L case is significantly increased. In addition, the time to peak is improved (in excess of 0.0001 seconds) while the entire transient event continues to occur within 0.1 seconds. Thus the peak pressure and volume for the High Performance case not only coexist at some moment in time, but also overlap for most of the transient event.

Linear Plot (Inclusion Only)

While the overall impact of changing the surrounding material may look minimal on a log plot, it is helpful to view the results with respect to a linear time scale (Figure 12).

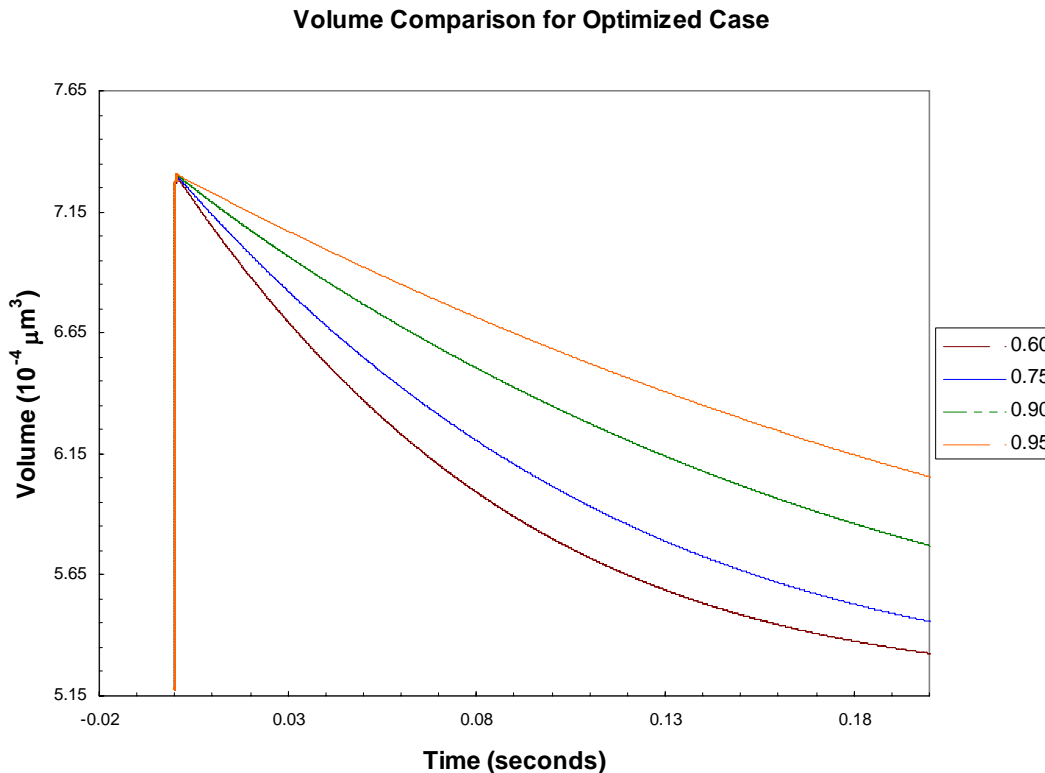


Figure 12 – Volume Expansion on a linear time scale

From this plot it is apparent that reducing the surrounding material has minimal impact on the initial rapid expansion, however the rate at which the inclusion relaxes back towards its initial

state is affected. From this we observe that the rate of volume decrease is directly dependent on the difference between the osmotic gradient pressure and the pressure generated through coupling the expansion with the surrounding material. The osmotic pressure quickly reaches a constant value, and the deformation dependent pressure will gradually decrease down to a value slightly above the osmotic constant pressure. With less surrounding polymer, this results in a much lower deformation pressure which leads to a slower relaxation of the inclusion.

Considering Pressure and Volume Together (Inclusion Only)

The results illustrated in Figure 11 show that reducing the volume fraction of the surrounding polymer (increasing R/L) has modest if any effect on peak volume, but peak pressure is significantly influenced by geometry; lower R/L ratios result in increased pressure. Increased pressure in the development of an actuator material is desirable, but intuitively, reducing the ratio too far will result in negligible expansion of the actuator as a whole. Thus, akin to other active materials there remains a trade off between blocked stress and free displacement that must be identified.

One of the most promising observations revealed in comparing the predictions for the Baseline versus the Increased Performance response of the inclusion, is that the total magnitude of free strain and blocked stress, as well as the time response of the peak values may be manipulated. Through this manipulation it may be possible to have an array of inclusions which will expand at tailored rates in relation to each other.

Transporter Current Response

The predicted current flows generated by the biological transporters and the flux of water across the membrane are illustrated in Figure 13. We note that due to the rapid establishment of the membrane potential, the cotransporters are able to maintain the constant pH gradient while pumping the water and sucrose into the inclusion faster than the fluid can diffuse out of the inclusion. This constant pH gradient allows the electric currents from the pumps, diffusion, and cotransporters to cancel each other.

The currents were examined at for two extremes in R/L ratios: .95 and .60. After comparing the two cases, it was found that the difference between the two was minimal. While decreasing the amount of surrounding polymer volume had an impact on the pressure-volume results, no changes were observed in the current flow. The current flows operate independently of the pressure and are functions only of the concentrations on either side of the membrane.

The Role of Membrane Permeability

Both the mechanical integrity and permeability of a naturally occurring BLM are insufficient for the needs of engineered active materials. However, it has been demonstrated that the proteins responsible for active response can be introduced into an artificial membrane, which introduces the potential for control over these basic membrane properties (Sundaresan and Leo, 2006b). The above study implicitly assumes that the mechanical integrity of the membrane matches (or is at least supported by) that of the surrounding polymer. The role of this property is considered here.

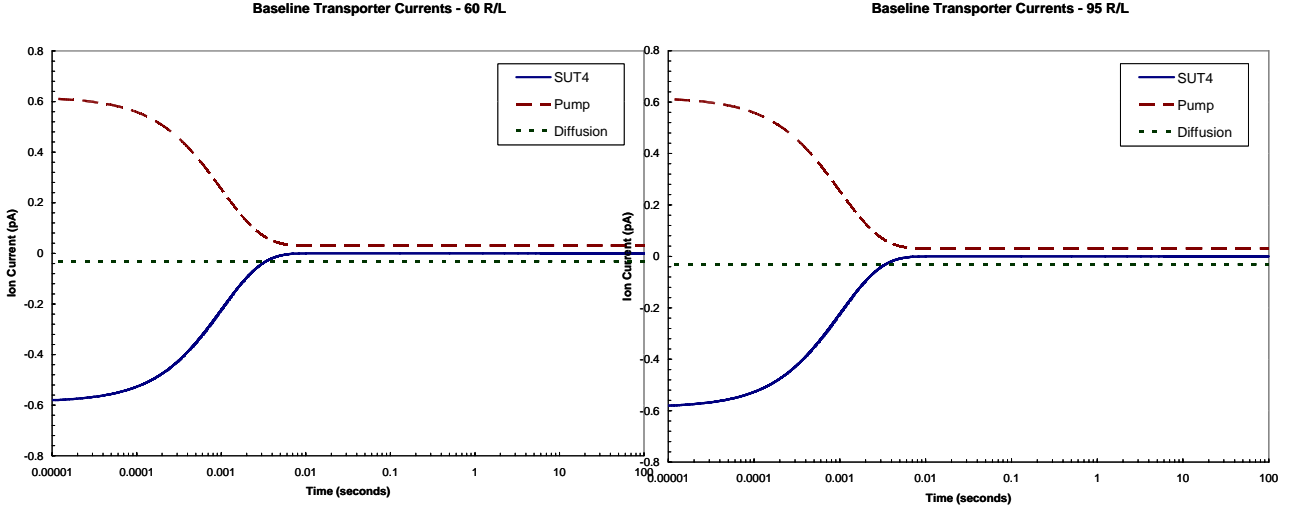


FIGURE 13 a-b – Baseline Transporter Currents

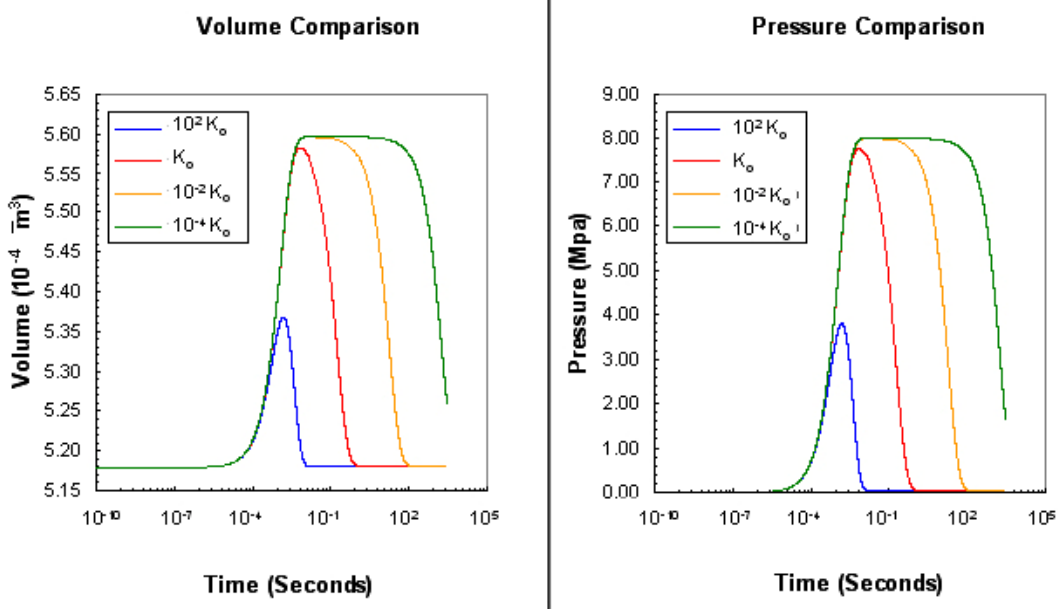


FIGURE 14A-B – Graphs of the pressure and volume results after varying the permeability of the membrane

Studies of BLM permeability in a $R/L = 0.50$ Baseline case predict that the time at peak will increase as permeability decreases, but little to no change in peak values is observed. Figure 14 illustrates the predicted effect of varying the permeability for the case of $R/L = 0.90$ where all other properties continue to correspond with the Baseline input parameters. In this study the baseline permeability of 1.65×10^{-15} is varied by factors of 10^{-4} , 10^{-2} , 10^0 , and 10^{+2} .

Increased permeability results in significant degradation of the inclusion response. However, the peaks in pressure and volume increase modestly for decreased permeability, while the time at peak is significantly increased (analogous to the results for the $R/L = 0.50$ case). The time to

peak continues to correspond with the Baseline rate of ~.01 seconds) for all cases. Similar trends are observed for the other geometries.

Based on these analyses, variation of BLM permeability may be used to tune the duration of the total actuation event with negligible impact on the magnitude of response.

Blocked Force Results (Actuator Configuration)

Blocked force calculations were obtained for three different R/L ratios. The values needed were determined through examining the stress results along the exposed edges of the finite element model, while the radius and thickness of the inclusions were pre-determined. After gathering the data for .75, .90, and .95 R/L values, the results were plotted. The values for .50 and .60 R/L were discarded due to high amounts of error, as the stress along the shell varied too intensely due to increased shell thickness.

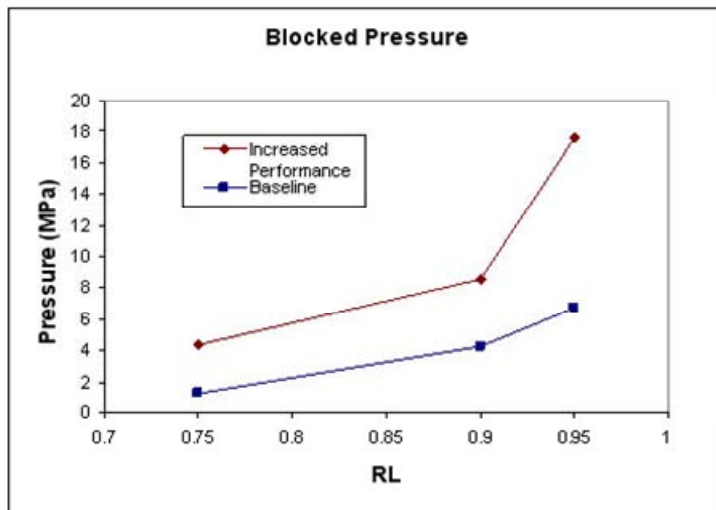


FIGURE 15 – Blocked Pressure vs. R/L .

Figure 15 illustrates that the peak blocked stress developed displays considerable variability with both geometry and initial system conditions. As expected, Increased Performance input parameters result in increased blocked stress; in addition, blocked stress increases as R/L decreases. Consideration of decreased permeability values results in the same predicted magnitudes already presented in Figure 15 (only the time that they are sustained is affected).

Free Displacement (Actuator Configuration)

The free displacement as illustrated in Figure 16 is easily determined from the finite element analysis for each case. Because of the small size of the model the parameter is presented in terms of free strain (divide by L) to enable comparison with other active materials. Figure 16 illustrates that the free strain is relatively insensitive to geometry for the cases considered here. As in the case of blocked pressure, decreased permeability values do not alter the magnitudes of the predicted free strain.

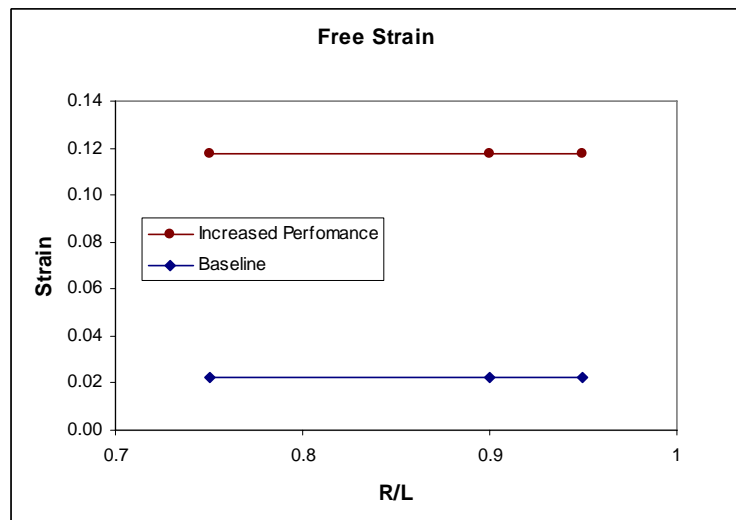


FIGURE 16 – Free Strain for fixed geometry and varied permeability

Impedance Matched Work (Actuator Configuration)

Using the results from the free displacement and blocked force studies, it is possible to determine the total work performed at both the inner membrane and the outer surface. Using equations from the modeling methodology section on impedance matched work, impedance matched work was determined for both the increased performance and baseline case with varying R/L ratios and differing membrane permeabilities.

Table 2 summarizes the impedance matched work predictions for the inclusion alone as well as the volume element as a whole for varied permeability, geometry, and input parameters. The mechanical properties of the surrounding polymer are held fixed in this analysis; ultimately this parameter will also play an important role in material system design.

TABLE 2 – Impedance Matched Work for Varied Permeability, Geometry, and Input Parameters.

Permeability	Impedance Matched Work (kJ/m ³)			
$10^{-4} K_0$	Increased Performance Parameters		Baseline Input Parameters	
	Model	Inclusion	Model	Inclusion
0.75	48	712	2.6	35.9
0.9	113	480	10.8	24.7
0.95	246	359	17.8	18.3
$10^{-2} K_0$				
0.75	48	712	2.6	35.8
0.9	113	480	10.8	24.6
0.95	246	359	17.8	18.3
K_0				
0.75	48	710	2.5	32.5
0.9	114	479	11.0	23.0
0.95	246	358	17.0	17.3
$10^2 K_0$				
0.75	45	627	~0	3.9
0.9	176	437	1.5	4.2
0.95	254	334	3.8	4.2

Plotting the increased performance and baseline cases for a standard permeability (K_0) with respect to R/L yields two important plots which convey the effectiveness of reducing the surrounding polymer.

In the previous section it is noted that the inclusion peak pressure increases as R/L decreases; however, by intuitive arguments as R approaches zero, progressively decreasing R/L cannot be representative of the optimum work available from the material. This argument is validated in the predictions of Table 2.

Consider one case of Increased Performance input parameters (shaded region in Table 2). As R/L decreases from 0.95 to 0.75 the work done by the inclusion nearly doubles. However, the reverse trend is observed for the volume element as a whole. If an ad hoc definition of efficiency is

imposed, this suggests that the efficiency for the $R/L = 0.75$ case is $\sim 7\%$ while the efficiency for the $R/L = 0.95$ case is $\sim 70\%$.

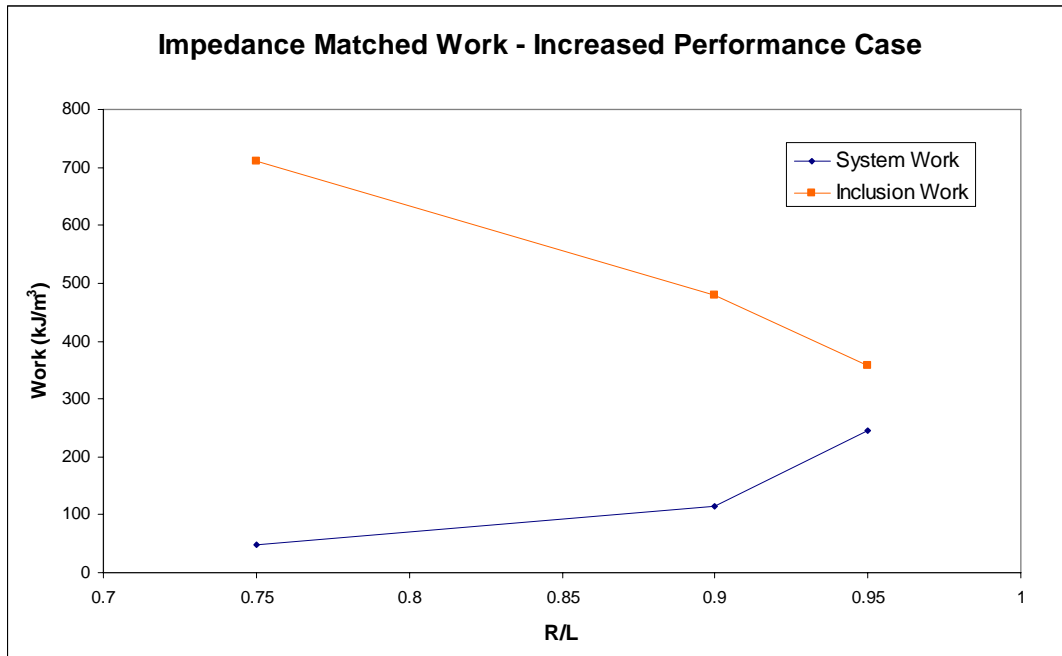


Figure 17a – Plot of the work done by the membrane (inclusion work) vs amount of work transmitted to the surroundings (system work) for the increased performance case. As the amount of surrounding material decreases (RL increases), the percentage of work transmitted from the inclusion to the system increases.

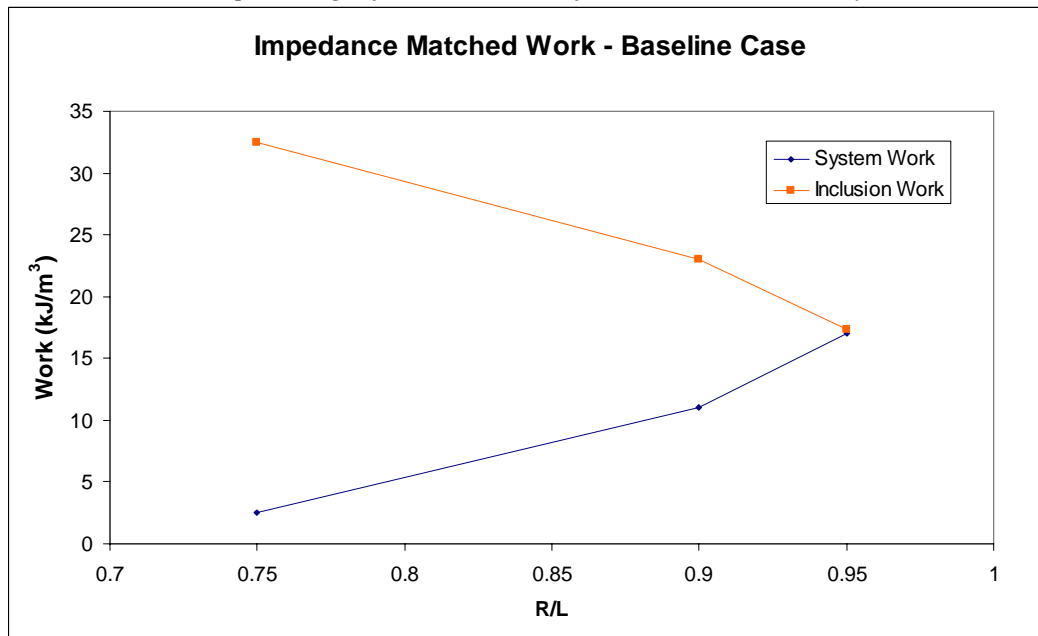


Figure 17b – Plot of the work done by the membrane (inclusion work) vs amount of work transmitted to the surroundings (system work) for the baseline case. As the amount of surrounding material decreases (RL increases), the percentage of work transmitted from the inclusion to the system increases.

In the earlier discussion of the effects of varied permeability, based exclusively on the reduced active response with increased permeability, it might have been tempting to presume increased permeability is always undesirable. However, for the High Performance input parameters, increased permeability also increases the “efficiency.” Thus, it is conceivable that increased permeability may be employed to tune both the magnitude and efficiency of response in the High Performance regime. (The predictions do not suggest that the same would be true for Baseline cases.)

Similarly, it is interesting to note that the efficiency of the response for Baseline input parameters is generally higher than that of the Increased Performance parameters; in some instances the efficiency is extraordinary, with a maximum of 98%.

It should be noted that the interpretation of efficiency addressed here should be approached with caution. A more appropriate definition of efficiency will examine the chemical energy required to stimulate the system. However, in the context of this report, which seeks primarily to define the role of material system design, such as geometry, the mechanical-to-mechanical efficiency offers appropriate insight.

While the impedance matched work is an important parameter, the rate of response is also of significant importance in active materials applications. Because the final state of the inclusion (species concentrations, etc.) has been significantly altered from its initialized state, this study neither confirms nor dismisses the possibility of sustaining a deformed state indefinitely through some controlled feed of ATP. Similarly, this study neither confirms nor dismisses the potential for cyclic response in this novel class of materials. However, this effort does suggest that the initial rate of response for the engineered material could be extraordinarily fast, while the deformed state could be held for orders of magnitude longer.

Example Implementation #2: Pharmaceutical Applications

All biological systems utilize various combinations of transport proteins penetrating a phase-separating bilayer membrane. Because the modeling construct developed as part of this research is generalized it could therefore be directly adapted to phenomena specific to the animal kingdom. One particularly intriguing adaptation includes applying the modeling concept to the creation of highly targeted drug or vaccine delivery. In this scenario the vesicle will contain a species requiring delivery to a specific location within the body. The application emphasis thus switches from repeatable expansion/contraction of an actuator to that of controlled burst to release the payload as needed. While the discussions presented in this section are still preliminary, the example applications are compelling. These include but are not limited to:

- Delivery of a chemotherapy drugs specifically at the site of a tumor, with *no* release of this poison elsewhere in the body;
- Release of pain-mitigation or any repeat-need drugs as needed (this represents a significant improvement over time release technology that inappropriately assumes some average rate of need); and
- Delivery of DNA-based vaccines for anthrax, cancer, etc. with dramatically superior effectiveness as compared to that of the current norm of protein-based vaccines.

The thought process underlying these applications is this - because transport protein based inclusions exhibit an on-trigger response, the inclusions will be stimulated to expand only in the presence of some predetermined trigger. In the tumor example, that trigger would be found only at the location of the tumor. In the as-needed drug delivery, all inclusions would respond to rising concentrations of some trigger. But if the inclusions were designed to burst at different rates, then the first round of burst would neutralize the trigger preventing further drug release. Similarly with the next round of release after the first round runs its course. In the case of vaccine delivery, a natural pH driven process known as endocytosis tends to degrade the vaccine prior to delivery at an appropriate intracellular location; in this case a quantifiable model projecting how variations in the chemical state interior to the inclusion combat this process will enable release of a fully functional payload. The following discussion and case study are still preliminary; the intent is to establish basic suitability of the modeling construct for projecting performance of drug/vaccine delivery strategies.

The Role of Endocytosis in Vaccine Delivery

The anthrax incidents in the Fall of 2001 underscored our current vulnerability to organized assaults with biological weapons. The relatively small initial amount of anthrax spores may have exposed up to 30,000 people, resulting in 5 deaths. In a more organized assault with aerosol form, the attack could be far more fatal.

While a vaccine for Anthrax was developed in 1970, this vaccine led to complaints of reactogenicity among its users. Several new delivery systems for the vaccine are currently being considered. One of the more promising techniques involves the intracellular delivery of peptides via genetic fusion with anthrax toxin. The success of this strategy hinges on developing a better understanding of the mechanism by which the vaccine reaches the cell nucleus, namely endocytosis (Brey, 2005). Similarly, the current proposed method for developing viable a cancer treatment involves introducing DNA based vaccines directly to the nucleus of affected cells.

For all approaches the vaccine is absorbed into the appropriate white blood cells through the process of endocytosis. In this process the cell extends and surrounds the vaccine for intake; the vaccine is then enclosed in an inclusion type known as an endosome. With the foreign species safely encased (similarly for a virus DNA or vaccine DNA), this endosome is then transported to the interior of the cell (Figure 18). While the endosome provides a convenient mode of transport for uptake, it also acts to destroy and break down its contents before releasing it into the cell through pH driving process. This natural process protects us from many pathogens, but serves as a barrier to successful DNA vaccine delivery. The vaccine must have some mechanism to release itself from the endosome before significant degradation occurs.

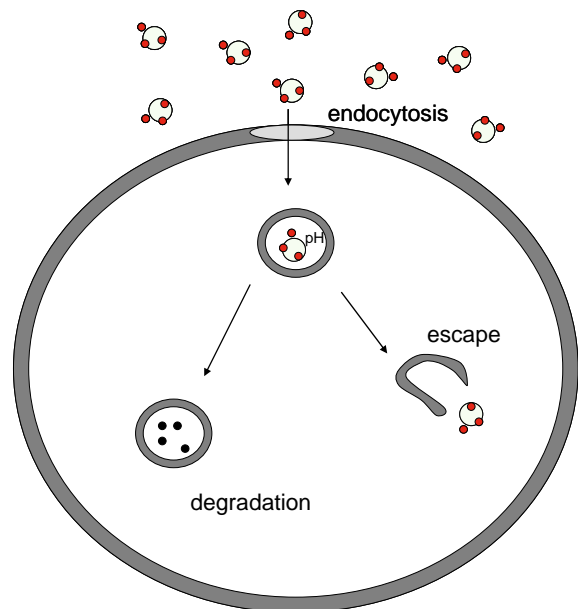


Figure 18 – Endocytosis

With the basic endocytosis process defined, consider next some details of how it occurs. Endosomes are the natural inclusions formed at the outer cell surface which take in and absorb material to be sorted and processed. During endocytosis, it has been observed that the inner pH of the endosome rapidly acidifies to 5 ± 0.2 . (Yamashiro et al. 1983). As the endosome travels down its channel, the internal pH will vary between 5-6 (Beaumelle, Hopkins, 1989). The mechanism for this acidification has been found to be ATP powered proton pumps which supply a constant influx of H^+ .

While much of the process is still unknown, it has been observed that endosomes themselves lack a cohesive shape or structure. The endosomal compartments involved in intracellular processing includes a very diverse collection of vesicular and tubular elements. The common trait of these endosomes is that the acidic pH in endosomes plays a critical role in mediating the orderly traffic of the receptors and ligands during the endocytosis process (Fuchs et al. 1988, Bramwell et al. 2004). Moreover, it has been established that ATP proton pumps are responsible for pH regulation, and that the small size of the endosomes enables the ATP pumps to maintain the pH required for this natural process. (Fuchs et al. 1988).

The foregoing discussion draws attention to a number of critical obstacles faced in the successful implementation of DNA-vaccine delivery that could be assessed via the nanoscale transport modeling construct. These issues include: the variations in endosome geometry, the importance of being able to quantify or even control the internal pH and rate of ATP proton pumping to prevent vaccine degradation, and the role of membrane properties including permeability and mechanical integrity. The following section offers a simple study on the role of geometry in inclusion (endosome) burst.

BURST PROFILES

In order to understand the role of geometry in burst, a number of inclusion sizes are considered simultaneously. The inclusions are ideally triggered by an external source, causing them to expand and eventually burst through gradually increasing surface area strain. The rate of release would be important, as only the required amount of material should be released.

Simplifying Assumptions:

For this study, the surrounding solid material is modeled as a cube. For this preliminary study of the applicability of the generalized modeling construct for the projection of pharmaceutical burst profiles a completely spherical casing would be more physically accurate. However, burst is projected per a maximum surface strain criterion which necessarily occurs at the thinnest region of the solid cross-section, and is relatively insensitive to the existence of thicker regions. Similarly, exact material burst properties are not available and thus the artificial membrane material properties are employed; this would tend to impact the exact time at which burst is predicted to occur, but the generalized trends will remain the same. The prediction times are therefore normalized.

The burst rate study employs geometry ratios; to achieve this, the original model is modified to incorporate a large range of different radii and distributions thereof, while maintaining the same membrane thickness. By varying both inclusion size and distribution of inclusion size, average time to burst is obtained through the area strain ratio. Projection of the burst profile required monitoring the predicted inclusion volume with respect to time in the simultaneous solution of equations; a specified burst strain of 1.2% is employed. This value is arbitrary but consistently employed to explore trends. Results are reported in terms of the percent of inclusion contents (volume) released for the total distribution of inclusions with respect to time (normalized with respect to total time in the absence of experimental validation).

Implementation:

The time to burst for each model was determined through a program written in visual basic embedded into Excel. This program is able to search through each of the space-delineated output files created by the UFLUID program and determine when the specified area strain was reached through comparing the initial volume to the current volume and calculating the strain from those values. After this strain was reached, the program reports the current value of time and continues onto the next model to check.

Table 3 – Burst prediction cases

	case 1	case 2	case 3	case 4	case 5
radius(10^{-8} m)	%comp	%comp	%comp	%comp	%comp
8	0.25	0.11	0.10	0.00	0.00
9	0.25	0.11	0.20	0.50	0.00
10	0.25	0.11	0.30	0.40	0.00
11	0.25	0.11	0.00	0.10	0.00
12	0.00	0.11	0.00	0.00	0.00
13	0.00	0.11	0.05	0.00	0.00
14	0.00	0.11	0.05	0.00	0.10
15	0.00	0.11	0.20	0.00	0.40
16	0.00	0.11	0.20	0.10	0.50

For the burst profile cases considered (Table 3), 9 different geometries were considered with radii ranging from 8×10^{-8} m to 16×10^{-8} m. Each of these geometries was simulated through the UFLUID under baseline conditions, with the conditions scaled by the new surface areas and volumes for the different inclusions. The volume predictions from each of these simulations were used to determine the length of time until the specified burst strain was reached. These compositions were combined with the time to burst strain to create the burst prediction plot below.

As these burst profiles demonstrate, inclusion geometry likely plays an important role in burst. Smaller radii were observed to initially expand more rapidly than the larger radii with an initial acceleration, but the overall increased performance of the larger inclusions rapidly overtook the smaller inclusions expansion as time went on. Therefore, specified burst strain is of considerable interest, because if a high value of strain is employed the larger inclusions will actually burst first. If a low value of strain is considered, the opposite is true. Membrane thickness may also play a large part in this study. The significance of this result is that considerable control over the release profile of the enclosed species exists simply via varying the inclusion size. Other control parameters include transporter density per unit surface area and concentration of ATP or similar stimulus.

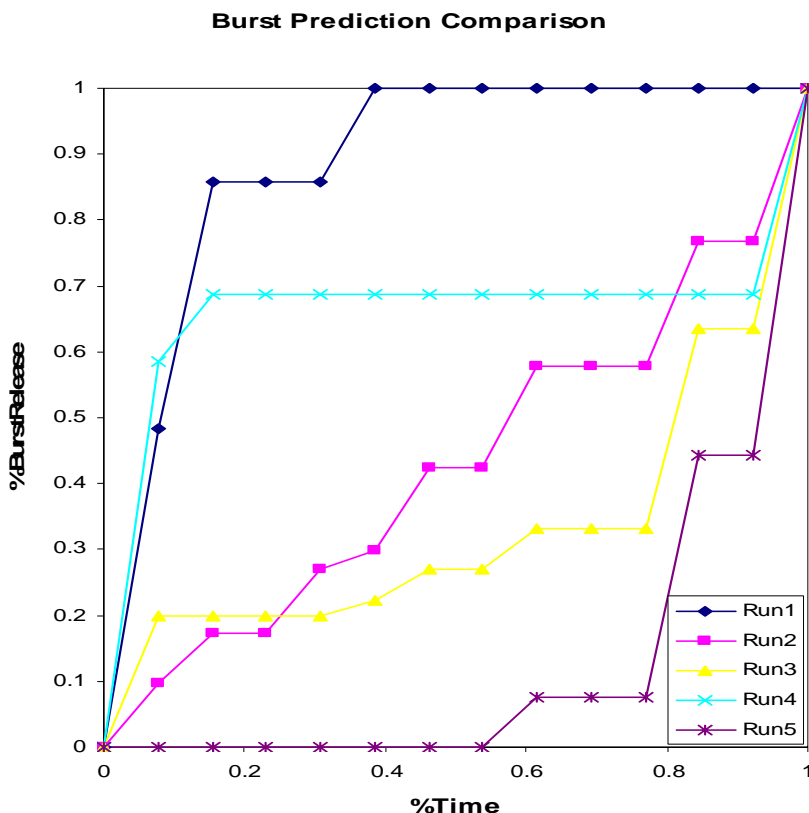


Figure 19 – Compilation of burst profiles.

Conclusions

A generalized modeling construct for active material systems based on nanoscale transport phenomena has been created. The approach couples bio-mimicking transport phenomena to the response of a host substrate. Application of the construct has been demonstrated in some detail for an example case of virtual design of a novel smart material. Utilizing this approach opens the opportunity to design novel active materials with dial-in stimulus, impedance matching properties, response rate, and response efficiency.

An alternate example case exploring use of the approach for pharmaceutical applications has also been offered. Even in the preliminary construct it becomes evident that the modeling construct enables quantified understanding of how to more effectively deliver drugs/vaccines. For instance, manipulation of inclusion geometry alone offers a mechanism to control delivery of drugs on an as-needed basis (as opposed to time release).

In general, the application range over which these examples span is intended to illustrate the versatility of the generalized construct. The modeling system is therefore ready to be employed to explore any number of specific applications in detail.

Bibliography

ABAQUS Analysis User's Manual, Vols. II, III, IV, and VI, 2004, ABAQUS, Inc., Providence, Rhode Island.

Beamelle, Bruno and Hopkins, Colin. 1989. "High yield isolation of functionally competent endosomes from mouse lymphocytes". *Biochem J.* Vol 264, pp 137-149.

Bonting, S. L., and de Pont, J. J. H. H. M., 1981, *New Comprehensive Biochemistry Volume 2 – Membrane Transport*, Elsevier, New York.

Bramwell, Vincent W, Eyles, Jim E., Alpar, H. Oya. 2005. "Particulate delivery systems for biodefense subunit vaccines." *Advanced Drug Delivery Reviews*, 57, pp 1247-1265.

Cadogan, David, Smith, Uhelsky, Frank, and MacKusick, Matt. "Morphing Inflatable Wing Development for Compact Package Unmanned Aerial Vehicles". 45th AIAA/ASME/ASCE/AHS/ASC Structures, Structural Dynamics and Materials Conference, Palm Springs, California, Apr. 19-22, 2004

Disalvo, A. Siddiqi, F. A., and Ti Tien, H, 1989. "Membrane Transport with Emphasis on Water and Nonelectrolytes in Experimental Lipid Bilayers and Biomembranes", In *Water Transport in Biological Membranes, Vol I*, Benga G., ed., CRC Press, Inc., Boca Raton, FL, pp. 41-75.

Endresen, L. P., 1997, "Chaos in weakly-coupled pacemaker cells", *J. Theor. Biol.*, 184, pp. 41 – 50.

Endresen, L. P., 2000, "Runge-Kutta formulas for cardiac oscillators", Institutt for fysikk, NTNU, N-7034 Trondheim, Norway.

Endresen, L. P., Hall, K., Høye, J. S., and Myrheim, J., 2000, "A theory for the membrane potential of living cells", *Eur. Biophys. J.*, 29, pp. 90 – 103.

Freeman, Eric, and Weiland, Lisa, 2008. "Applications of Biologically Inspired Membranes", *Proc of SMASIS*, Oct 28-30, Ellicott City, MD.

Freeman, Eric, and Weiland, Lisa, 2007, "Parametric Studies of a Coupled Transport/Hyperelastic Model for High Energy Density Nastic Materials", *Proc of ASME-IMECE*, Nov 14-16, 2007, Seattle, WA.

Freeman, Eric and Weiland, Lisa, 2008. "High Energy Density Nastic Materials: Parameters for Tailoring Active Response". *In press*, *Journal of Intelligent Material Systems and Structures*.

Fuchs, Renate, Male, Phillipe, and Mellman, Ira. 1988. "Acidification and Ion Permeabilities of Highly Purified Rat Liver Endosomes." *The Journal of Biological Chemistry*, 264, pp 2212-2220.

Hodgkin, A. L., and Huxley, A. F., 1952, “A Quantitative Description of Membrane Current and its Application to Conduction and Excitation in Nerve”, *J. Physiol.* (London), 117, pp. 500 – 544.

Hodgkin, A. L., Huxley, A. F., and Katz, B., 1952, “Measurement of Current-Voltage Relations in the Membrane of the Giant Axon of Loligo”, *J. Physiol.* (London), 116, pp. 424 – 448.

Homison, C, 2006, “Coupled Transport/Hyperelastic Model for High Energy Density Nastic Materials”, University of Pittsburgh Masters Thesis.

Homison, C. and Weiland, L. M., 2005, “Coupled Transport/Hyperelastic Model for Nastic Materials”, Proc. Of ASME – ISME, Nov. 5 – 11, 2005, Orlando, FL.

Homison, C. and Weiland, L.M., 2006, “Coupled Transport/Hyperelastic Model for Nastic Materials,” Proc. SPIE, San Diego, CA, March 2006

Jeerage, Kavita M, Noble, Richard D., and Koval, Carl A. 2007. “Investigation of an aqueous lithium iodide/triiodide electrolyte for dual chamber electrochemical actuators”. *Sensors and Actuators B* 125, 2007, pp 180-188.

Luo, Don and Saltzman, W. Mark. 2000. “Synthetic DNA Delivery Systems.” *Nature Biotechnology*, Vol 18.

Mathews, L, Sundaresan, V.B., Giurgiutiu, V, and Leo, D.J., 2006a, “Bioenergetics and mechanical actuation analysis with membrane transport experiments for use in biomimetic nastic structures,” *J. Mater. Res.* 2006; 21(8); 2058-2067.

Mathews, L, Giurgiutiu, V. 2006b. “Modeling Actuation Forces and Strains in Nastic Structures”. *Smart Structures and Materials 2006: Smart Structures and Integrated Systems – SPIE*, Volume 6173, pp. 502-511.

Mauck, Lisa D, and Lynch, Christopher H, 2000, “Piezoelectric Hydraulic Pump Development,” *J. Intelligent Materials Systems and Structures*, 11, pp 758-764.

Mullins, L. J., 1977, “A Mechanism for Na/Ca Transport”, *J. Gen. Physiol.*, 70, pp. 681 – 695.

Mullins, L. J., 1981, *Ion Transport in Heart*, Raven Press, New York.

Newnham, R. E., 1992, “Piezoelectric Sensors and Actuators: Smart Materials”, Proc of 46th IEEE Frequency Control Symposium, May 27-29, 1992, Hershey, PA, pp 513-524

Oates, W. S., Mauck, L. D., and Lynch, C. S., 2000, “PZT piston driven hydraulic pump development”, Proc of 12th IEEE International Symposium on Applications of Ferroelectrics, Jul 21-Aug 2, 2000, Honolulu, HI, 2, pp 733-736.

Philen, MK et al 2007. “Fibrillar Network Adaptive Structure with Ion-transport Actuation”. *Journal of Intelligent Material Systems and Structures*. Vol 18, April 2007, pp 323-334.

Ries, R. S., Choi, H., Blunck, R., Beznilla, F., and Heath, J. R. 2004, “Black Lipid Membranes: Visualizing the Structure, Dynamics, and Substrate Dependence of Membranes”, *J. Phys. Chem. B*, **108**, pp 16040-16049

Robinson, R. A., and Stokes, R. H., 1965, *Electrolyte Solutions*, Butterworths, London.

Schultz, S. G., 1980, *Basic Principles of Membrane Transport*, Cambridge University Press, New York.

Stein, W. D., 1989, “Kinetics of Transport: Analyzing, Testing, and Characterizing Models Using Kinetic Approaches”, In *Methods in Enzymology* Vol. 171, Part R, Transport Theory: Cell and Model Membranes, Abelson, J. N. and Simon, M. I., eds., Academic Press, San Diego, CA, pp 23-62.

Su, Y., Lin, L., and Pisano, A., 2002, “A Water-Powered Osmotic Microactuator”, *J. Microelectromechanical Systems*, 11(6), pp. 736 – 742.

Sundaresan, V. B. and Leo, D. J., 2007, “Biological Ion Transporters as Gating Devices for Chemomechanical and Chemoelectrical Energy Conversion”, Virginia Polytechnic Institute and State University, Virginia.

Sundaresan, V.B., Homison, Chris, Weiland, L.M., and Leo, D.J., 2007, "Biological Transport Processes for Microhydraulic Actuation," *Sensors and Actuators B: Chemical*, [Vol 123, Iss 2](#), 21 May 2007, pp 685-695 .

Yamashiro, Darrel, Fluss, Sharon R and Maxfield, Frederick, 1983. “Acidification of Endocytic Vesicles by an ATP-dependent Proton Pump”. *J of Cell Biology*, Vol 97, pp 929-934

